

Key Points:

- First Time-dependent multi-stream electron transport calculations are presented
- Intensity modulation variations for emissions at 4,278, 6,730, 7,774 and 8,448 Å during flickering aurora are compared
- Time-shift between column emission rates at 4,278, 6,730, 7,774 and 8,448 Å are predicted

Supporting Information:

Supporting Information may be found in the online version of this article.

Correspondence to:

B. Gustavsson,
bjorn.gustavsson@uit.no

Citation:

Gustavsson, B. (2022). Time-dependent electron transport I: Modelling of supra-thermal electron bursts modulated at 5–10 Hz with implications for flickering aurora. *Journal of Geophysical Research: Space Physics*, 127, e2019JA027608. <https://doi.org/10.1029/2019JA027608>


Received 7 NOV 2019

Accepted 16 JAN 2020

© 2022 The Authors.

This is an open access article under the terms of the [Creative Commons Attribution-NonCommercial License](https://creativecommons.org/licenses/by-nc/4.0/), which permits use, distribution and reproduction in any medium, provided the original work is properly cited and is not used for commercial purposes.

Time-Dependent Electron Transport I: Modelling of Supra-Thermal Electron Bursts Modulated at 5–10 Hz With Implications for Flickering Aurora

B. Gustavsson¹ 

¹UIT, The Arctic University of Norway, Tromsø, Norway

Abstract A time-dependent multi-stream electron transport model, AURORA, has been developed for studies of auroral emission-rates during precipitation with large variations on sub-second time-scales. The transport-code accurately takes time-of-flight, energy degradation, scattering and production of secondary electrons into account. AURORA produces ionospheric electron-flux as a function of energy, altitude, time and pitch-angle, with a time-resolution of 3.33 ms. AURORA has been used to simulate flickering aurora by modulating field-aligned bursts (FAB) of electrons modulated at frequencies between 5 and 10 Hz. Intensity modulations of auroral emissions at 4,278, 6,730, 7,444, and 8,446 Å have been calculated, time-shifts on the order of 10 ms between the maxima of the emissions were found.

Plain Language Summary Sometimes the polar auroras vary in intensity at sub-second time-scales. To calculate the auroral brightness for such fast variations it is necessary to take into account the time it takes high-energy electrons to move from the source-altitude (typically a few thousand kilometers) down to and through the upper atmosphere (down to about 100 km altitude), and the time it takes for these electrons to lose their energy. Here we present a model “auroral electron-transport” that takes these effects into account. One of the results of this model is that we predict small time-shifts between auroral emission.

1. Introduction and Background

The aurora is the most spectacular natural phenomena that directly displays the dynamics of the interactions between the solar wind, the magnetosphere and Earth's upper atmosphere. Several auroral phenomena display significant intensity variations at sub-second time-scales, such as flickering aurora where the intensity varies in complex rotating and swirling patches, typically at frequencies between 5 and 15 Hz (Gustavsson et al., 2008; Michell et al., 2012; Sakanoi & Fukunishi, 2004; Whiter et al., 2010), flaming auroral rays, with intensity enhancements moving up (and down) the rays at sub-second time-scales (Blixt et al., 2005; Dahlgren et al., 2013; Grydeland et al., 2004), filamenting auroral arcs where small-scale auroral arcs filament into smaller and smaller arc-lets over a couple of seconds (Semeter & Blixt, 2006), curls (Vogt et al., 1999) and even smaller-scaled boundary undulations (Dahlgren et al., 2010) rapidly moving along the edges of auroral arcs. For auroras that dynamic, neither the fluxes of primary high-energy electrons nor secondary low-energy electrons are at steady-state since the precipitation varies on time-scales which are short compared to the trans-ionospheric travel-time and energy degradation-time, respectively. To model the ionospheric responses to electron-precipitation with sub-second variations time-dependent electron transport calculations have to be used, regardless of the source process producing the energy–pitch-angle distribution of the primary precipitating electrons that cause the different dynamic aurorae. In their ground-breaking work with the first time-dependent electron-transport calculations, Peticolas and Lummerzheim (2000) modeled the 4,278 Å emission from N_2^+ produced by wide-energy-dispersed strictly field-aligned bursts (FAB) of electrons modulated at 5 and 100 Hz. This electron spectrum was chosen to model the precipitation of electron-beams with narrow pitch-angle extent with electron-fluxes modulated from low energies up to a few keV similar to what has been observed in situ above flickering aurora (e.g., McFadden et al., 1987). At the time (1999–2000) Peticolas and Lummerzheim had to make some simplifying approximations to make the problem computationally tractable. The two major simplifications were: (a), to restrict the model to strictly field-aligned primary high-energy electrons, ignoring pitch-angle re-distribution by elastic scattering and, (b), to model fluxes of secondary electrons at energies below 100 eV in a “local approximation” ignoring transport. A model with these approximations ignore back-scattering of primary electrons out of the ionosphere and the transport of secondary electrons, primarily upward from E-region altitudes. Both of these effects are small, at

least for field-aligned precipitation. For rapidly varying primary precipitation with wider pitch-angle distribution, as has been observed for example, by Arnoldy et al. (1999); these effects should be accounted for, even though the modulation of ionospheric responses would be reduced for rapidly varying precipitation launched over a wide range of pitch-angles—since the increased range of field-aligned velocities would lead to a rapid spread of E-region (low-altitude) time-of-arrival.

Before developing a general time-dependent electron transport code, it is worthwhile to consider the pros and cons of modifying current methods of calculating the ionospheric response to particle precipitation for steady-state conditions. Such methods can be separated into three broad groups: range–energy-deposition models (e.g., Fang et al., 2010; Rees, 1989; Sergienko & Ivanov, 1993), Monte Carlo-based methods (e.g., Gattinger et al., 1996; Sergienko & Ivanov, 1993; Solomon, 1993), and multi/two-stream models (e.g., Lummerzheim & Lilensten, 1994; Stamnes, 1981; Strickland et al., 1989). These methods are all adequate for steady-state conditions, with slightly different strengths. Here we will briefly discuss pros and cons of extending them to handle time-dependent electron precipitation. In order to extend Monte-Carlo-method of electron transport, the main modification is to include tracking the time of propagation between collisions of the electrons. This should be a minor modification from a physics point of view, to also store the electron time-of-flight might become computationally challenging in practice, but no additional approximations are required. The results will be limited by statistical fluctuations and counting-noise. To adapt a multi-stream model for steady-state conditions to a time-dependent model, we should note that a steady-state code solves systems of coupled ordinary differential equations for altitude-variations of electron-flux-profiles, this has to be modified to integration of coupled partial differential equations to calculate the altitude and time-variation of electron fluxes. The range–energy-deposition models are less directly extendable to account for time-variation. Mathematically these models can be described as “reduced impulse-response” models in the meaning that for given input electron spectra, $I_e(E, \theta)$, the altitude-profile of the ionospheric responses (ionization rate, $q_e(z)$, excitation rates, $q_\lambda(z)$) are calculated. The procedure can in principle be extended to produce the altitude-time responses ($q_e(z, t)$, $q_\lambda(z, t)$) but much of the gain in mathematical simplicity would be lost.

In this paper, we present time-dependent electron transport modeling of optical emissions for electron precipitation modulated at 5, 7 and 10 Hz. The primary electron spectra used are FAB, with constant flux from 100 eV up to 3, 5 and 7 keV. For this purpose we have developed a time-dependent multi-stream electron transport model, AURORA. AURORA takes time-of-flight for electron-fluxes at different pitch-angles into account and properly models the time-variation of scattering and energy degradation caused by inelastic collisions and ionization. For validation we compare it with the results of Peticolas and Lummerzheim (2000). Electron spectra, both pitch-angle resolved and hemispheric are modeled, allowing for direct comparison with in-situ observations. Excitation-rates and column emission-rates for optical emissions from atomic oxygen, molecular nitrogen, and molecular nitrogen ions are calculated and relative intensity modulation and time-shifts between auroral emissions are compiled to allow for comparisons with optical observations of flickering aurora. However, the predicted time-shifts are on the order of a few ms, this makes it difficult to make comparisons with existing observations, for example, Kataoka et al. (2011) have presented multi-wavelength observations of flickering aurora with camera synchronization uncertainties less than 10 ms. To resolve time-shifts on the order of a few ms the synchronization uncertainty has to be less than 100 μ s, this will be a challenge. The term electron flux in electron transport studies refers to the number of electrons passing through a unit surface and unit solid angle per energy and time. In this paper, this term is used synonymously with differential electron flux in rocket and satellite measurements.

2. Time-Dependent Multi-Stream Electron Transport Equation

The temporal and spatial variation of energetic electron fluxes in the ionosphere can be modeled with the Boltzmann equation for phase-space density. Since the electron transport is much smaller perpendicular to the magnetic field than parallel with it, we can simplify the problem to a one-dimensional Boltzmann equation by only accounting for field-aligned motion of electrons (e.g., Guio, 1998; Schunk & Nagy, 2009):

$$\frac{\partial f}{\partial t} + \mu v \frac{\partial f}{\partial s} + \frac{q_e}{m} \mathbf{E}_{\parallel} \mu \frac{\partial f}{\partial v} + \left(\frac{q_e}{m} \mathbf{E}_{\parallel} - \frac{v^2}{2B} \frac{dB}{ds} \right) \frac{1 - \mu^2}{v} \frac{\partial f}{\partial \mu} = \frac{\delta f}{\delta t}_{coll} \quad (1)$$

where f is the phase-space density, t is the time, s is the distance along the magnetic field, v is the velocity, $\mu = \cos\theta$ where θ is the pitch-angle, E_{\parallel} is the electric-field component along the magnetic field, and B is the magnetic field-strength. After making the approximation that the field-aligned electric field component and the converging magnetic field have a negligible effect on f in the ionosphere (Peticolas & Lummerzheim, 2000) and transforming coordinates from velocity to energy and from distribution function to electron flux we arrive at the time-dependent electron transport equation

$$\frac{1}{v(E)} \frac{\partial I(E, s, \mu, t)}{\partial t} + \mu \frac{\partial I(E, s, \mu, t)}{\partial s} = -A I(E, s, \mu, t) + B(E, s, \mu, t, I) + Q(E, s, \mu, t, I) + n_e \frac{\partial (L_{ee}(E) I(E, s, \mu, t))}{\partial E} \quad (2)$$

The first term on the right-hand side represents losses of electron flux from energy, E , and pitch angle-cosine, μ , due to elastic collisions changing the pitch angle and by inelastic collisions changing energy and possibly pitch-angle, with

$$A = \sum_k n_k(s) \sigma_k^{tot}(E)$$

where $\sigma_k^{tot}(E)$ is the total cross section for collisions of electrons at energy E with the k -th species. From here on, k, j, i , and l will be used as indices; they are not used as unique identifiers. The second term on the right-hand side represents elastic scattering of electrons from other pitch angles, μ' , to pitch angle μ :

$$B(E, s, \mu, t, I) = \sum_k n_k(s) \sigma_k^{el}(E) \cdot \int_{-1}^1 p_k^{el}(E, \mu' \rightarrow \mu) I(E, s, \mu', t) d\mu'$$

where $p_k^{el}(E, \mu' \rightarrow \mu)$ is the probability that an electron at energy E with pitch angle μ' will scatter to pitch angle μ for elastic collisions with particles of species k . To calculate these probabilities we use phase-functions derived from Porter et al. (1987) extended and updated with data from Linert et al. (2004) for molecular oxygen and Kanik et al. (2001) for atomic oxygen. The third term on the right-hand side, $Q(E, s, \mu, t, I)$, combines all internal sources of energetic electrons, that is, production of photo-electrons and secondary electrons, and electrons cascading to energy E from higher energies, ε , due to inelastic collisions:

$$Q(E, s, \mu, t, I) = Q_{local}(E, s, \mu, t) + \sum_k n_k(s) \sum_j \sigma_k^j(\varepsilon \rightarrow E) \int_{-1}^1 p_k^j(\varepsilon, \mu' \rightarrow \mu) I(\varepsilon, s, \mu', t) d\mu' + \sum_k n_k(s) \int_{E+E^*}^{\infty} \sigma_k^{ion}(\varepsilon \rightarrow E) \int_{-1}^1 p_k^{ion}(\varepsilon, \mu' \rightarrow \mu) I(\varepsilon, s, \mu', t) d\mu' d\varepsilon \quad (3)$$

where the summations in the second term are over all the excited states j of the k -th species. Electrons exciting an atom or a molecule lose a quanta of energy corresponding to the excitation energy, ΔE . Therefore electrons at energy ε that collide inelastically will contribute to the second term of Q at a series of discrete energies, $E = \varepsilon - \Delta E_k^j$ corresponding to the excitation thresholds of neutral species k . In ionizing collisions, represented with the third term in Equation 3, the energy loss of primary electron is the sum of the ionization energy and the energy of the secondary electron. The fourth term on the right-hand side of Equation 2 accounts for the loss due to energy transfer to ambient electrons of density $n_e(s)$ and temperature T_e (Swartz et al., 1971). Since the flux $I(E, s, \mu, t)$ depends not only on fluxes at all higher energies but also on fluxes with all other pitch-angles Equation 2 has to be solved simultaneously in a set of coupled PDEs for all pitch-angles, combined with the corresponding initial and boundary conditions. The boundary condition at the upper boundary are typically time-variations of downward fluxes at all energies and pitch-angles, either obtained from observations or simulations, or chosen (more arbitrarily) for modeling. For the upward fluxes the “most natural” boundary-condition is to set the gradients to zero —since the scattering decreases with the exponentially decreasing neutral density and the upper boundary is at an altitude where the scattering is negligibly small. The lower boundary is best handled by using an altitude

low enough that the fluxes are so negligibly small that we can set the boundary condition for all pitch-angles and energies to zero.

Energetic electrons effectively only undergo energy degradation in the ionosphere—also for the time-dependent case. A consequence of this is that we can solve Equation 2 from the highest energy, for which Q is zero, and then calculate all the fractions of electrons that collide inelastically and degrade to lower energies which gives us the contributions to $Q(E, s, \mu, t, I)$ for all (E, s, μ, t) , and then proceed to iteratively solve Equation 2 for the next lower energy.

To solve the set of Equation 2 we discretize in energy, with an n_E element non-uniform energy-grid from 2 eV to the highest energy and divide the flux into n_μ discrete pitch-angle-bins, covering pitch-angles from 0 to 180°, or from $\mu = -1$ to $\mu = 1$, with pitch-angle limits $\tilde{\mu}_0, \tilde{\mu}_1, \dots, \tilde{\mu}_{n_\mu+1}$. The first step toward a discretized version of Equation 2 is to rewrite the energy differential describing the electron-electron collisions. For the time-dependent electron transport this is most clearly written as

$$n_e \frac{\partial (L_{ee}(E)I(E, \mu))}{\partial E} \rightarrow \frac{1}{v(E_{i+1})} \frac{\partial \epsilon_{ee}}{\partial t} \frac{I^{\mu_i}(E_{i+1})}{\Delta E_{i+1}} - \frac{1}{v(E_i)} \frac{\partial \epsilon_{ee}}{\partial t} \frac{I^{\mu_i}(E_i)}{\Delta E_i} \quad (4)$$

Here $\partial \epsilon_{ee} / \partial t$ is the electron energy-loss-rate (Swartz et al., 1971):

$$\frac{\partial \epsilon_{ee}}{\partial t} = \frac{3.0271 \cdot 10^{-10} n_e^{0.97}}{E^{0.44}} \left(\frac{E - E_e}{E - 0.53 E_e} \right)^{2.36} \quad (eV/s)$$

where n_e and E_e are the electron density (in m^{-3}) and the thermal energy (in eV) respectively and E is the electron energy (in eV). The second term in the discretized form for electron-electron loss in Equation 4 is a linear loss term for electron flux at E_i and can be merged into A in Equation 2 (e.g., Gronoff et al., 2012), while the first term is a source of electrons to energy-bin E_i from the next higher energy-bin, which can be added to Q in Equation 3. This turns Equation 2 into an equation for the stream μ_i with pitch-angle-cosines from $\tilde{\mu}_i$ to $\tilde{\mu}_{i+1}$:

$$\begin{aligned} \frac{1}{v(E_i)} \frac{\partial I^{\mu_i}(E_i, s, t)}{\partial t} + \bar{\mu}_i \frac{\partial I^{\mu_i}(E, s, t)}{\partial s} = & -A' I^{\mu_i}(E_i, s, t) \\ & + \sum_{\mu_k} B'(E, s, \mu_k \rightarrow \mu_i) I^{\mu_k}(E_i, s, t) \\ & + Q'(E_i, s, \mu_i, t) \end{aligned} \quad (5)$$

where $\bar{\mu}_i$ is the average of the pitch-angle-cosine for electrons in stream i , that is,

$$\bar{\mu}_i = \frac{\int_{\theta_i}^{\theta_{i+1}} \cos \theta \sin \theta d\theta}{\int_{\theta_i}^{\theta_{i+1}} \sin \theta d\theta}$$

Here we assume that the electron flux inside a pitch-angle stream is isotropically distributed between its pitch-angle limits. In this discretized version of the transport equation A' is the sum of the neutral densities multiplied with the total collision cross-section and the electron-electron loss-rate, in the second term on the right-hand side, B' is slightly modified to account for both the discretization in μ as well as correcting for the fact that a fraction of the inelastic collisions, with excitation energy ΔE_k^j , will lead to energy degradation to energies between E_i and $E_i + \Delta E_i^j$; and to account for scattering from all pitch-angles in streams μ_i to all pitch-angles in stream μ_i :

$$\begin{aligned} B'(E_i, s, \mu_i \rightarrow \mu_i) = & \sum_k n_k(s) \sigma_k^{el}(E_i) \int_{\tilde{\mu}_i}^{\tilde{\mu}_{i+1}} \int_{\tilde{\mu}_i}^{\tilde{\mu}_{i+1}} p_k^{el}(E_i, \mu' \rightarrow \mu) I(E_i, s, \mu', t) d\mu' d\mu + \\ & \sum_k n_k(s) \sum_j \sigma_k^j(E_i) \int_{\tilde{\mu}_i}^{\tilde{\mu}_{i+1}} \int_{\tilde{\mu}_i}^{\tilde{\mu}_{i+1}} p_k^j(E_i, \mu' \rightarrow \mu) I(E_i, s, \mu', t) d\mu' d\mu \cdot \\ & \max(0, 1 - \Delta E_k^j / \Delta E_i) . \end{aligned} \quad (6)$$

Q' is modified correspondingly.

Equation 5 still has to be solved simultaneously in a set with similar equations for all streams, μ_j , but with the discretization into pitch-angle-streams we can now write the full set of Equation 5 for all pitch-angle streams:

$$\frac{1}{v} \frac{\partial}{\partial t} \begin{bmatrix} I^1 \\ I^2 \\ \vdots \\ I^n \end{bmatrix} + \frac{\partial}{\partial s} \begin{bmatrix} \bar{\mu}_1 I^1 \\ \bar{\mu}_2 I^2 \\ \vdots \\ \bar{\mu}_n I^n \end{bmatrix} = \begin{bmatrix} -A' + B'_{11} & B'_{21} & \cdots & B'_{n1} \\ B'_{12} & -A' + B'_{22} & \cdots & B'_{n2} \\ \vdots & \vdots & \ddots & \vdots \\ B'_{1n} & B'_{2n} & \cdots & -A' + B'_{nn} \end{bmatrix} \begin{bmatrix} I^1 \\ I^2 \\ \vdots \\ I^n \end{bmatrix} + \begin{bmatrix} Q^1 \\ Q^2 \\ \vdots \\ Q^n \end{bmatrix} \quad (7)$$

Here I^k is an n_z -column-array with altitude-variation of electron flux in stream k at time t . The matrix on the right-hand side is $(n_z n_\mu \times n_z n_\mu)$ composed of n_μ by n_μ diagonal sub-matrices (of size $n_z \times n_z$), A' with the altitude-varying total collision cross-section, and B'_{jl} with the collisional scattering from stream j to stream l – the sum of the elastic collisions and the fraction of inelastic collision that lead to the electrons maintaining an energy between E_i and $E_i + \Delta E_i$. Integration of Equation 7 is done with a standard Crank-Nicolson scheme modified to use up-stream spatial differences instead of centralized spatial differences. The boundary conditions have to be imposed for the first and last component of each of the sub-arrays I^k . To ensure stability of the solution for any type of discontinuous changes in I^k the time-step, Δt , of the Crank-Nicolson integration are chosen such that the Courant-number, $|v(E_i)\Delta t/\Delta s|$, is smaller than 1 at all energies. Further, a requirement for the discretization is that Δs should not be larger than the electron mean-free-path. This we achieve by applying an approximately 150 m step-size in altitude from 100 to 140 km transitioning to an exponentially growing step-size to the highest altitude at 649 km. The two primary consequences of these design-choices are, first, that for high-energy electrons the step-size in time becomes so short ($\approx 3 \mu s$, for 7 keV electrons), i.e., is both computationally impossible and physically irrelevant to save the solution at every time-step of the integration – instead the solution is stored with time-resolution of 1–20 ms. Second, that it is difficult to model precipitation with energies much larger than 10 keV since that would require a lower border at an altitude below 100 km, where the electron mean-free-path is rapidly decreasing – which would necessitate a much finer altitude-grid, leading to a significant reduction of the time-step in the Crank-Nicolson integration. With all these considerations, the number of pitch-angle streams, n_μ , that currently can be handled with a standard 2016 desktop computer in a reasonable time is approximately 10, this limits how well smooth pitch-angle distributions can be modeled at this point in time. In this work we used 10 pitch-angle-streams with pitch-angle boundaries at $0^\circ, 10^\circ, 30^\circ, 60^\circ, 80^\circ, 90^\circ, 100^\circ, 120^\circ, 150^\circ, 170^\circ$ and 180° from **B**.

The field-aligned velocity components, v_{\parallel} , of electrons in a energy and pitch-angle cell, $[E_i, E_i + dE_i) \times [\mu_j, \mu_j + \Delta\mu_j)$, will have a spread such that

$$v(E_i) \mu_{j+1} \leq v_{\parallel} \leq v(E_i + dE_i) \mu_j$$

where $v(E)$ is the velocity of electrons with energy E . For 1 keV electrons this leads to a 1.0 per cent spread around the average field-aligned velocity component in the 0° – 10° stream, a 6.7 percent spread in the 10° – 30° stream, which both are unproblematic. For electrons in the 30° – 60° stream the spread grows to 27 per cent, which makes the assumption that all electrons in an energy and pitch-angle cell moves with the average field-aligned velocity problematic. To mitigate this problem a small diffusive term, with pitch-angle and energy-varying diffusivity, is added to the right-hand-side matrix in Equation 7. In addition to account for the variation in field-aligned velocity, multiple pitch-angle streams are required to accurately model the length-distribution of electron-trajectories through the ionosphere, which impacts the ionization and excitation profiles. This aspect of the electron transport the 10-stream calculation accounts for well. Finally, a large number of pitch-angle streams are necessary to model precipitation with general pitch-angle distributions – with 10 streams with pitch-angle boundaries at $0^\circ, 10^\circ, 30^\circ, 60^\circ, 80^\circ, 90^\circ, 100^\circ, 120^\circ, 150^\circ, 170^\circ$ and 180° from **B** this is impossible to do well, a far larger number of streams is required to keep the solid-angles of the streams reasonably similar. The 10-streams used is sufficient for modeling precipitation that is either isotropic or field-aligned to within 10° or 30° from **B**.

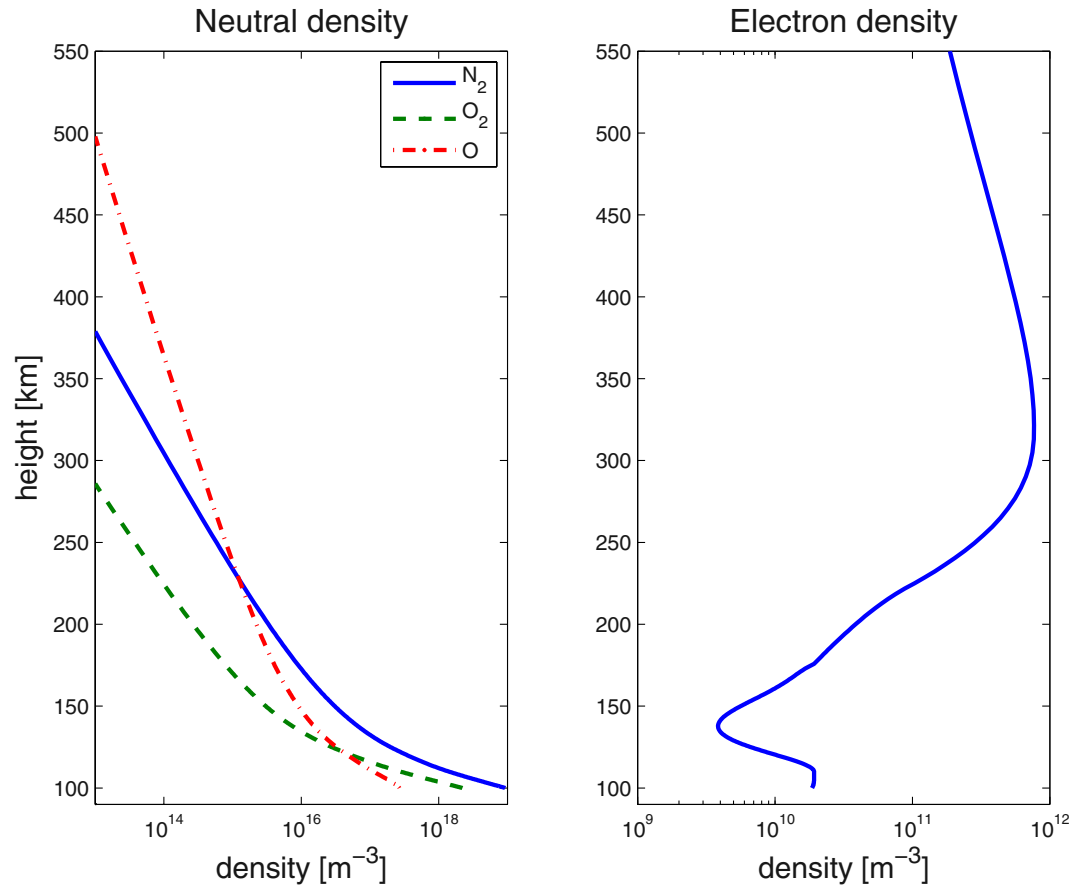


Figure 1. The density profiles for the major thermospheric constituents used are shown in the left panel. The right panel displays the electron density profile.

3. Comparison With Peticolas and Lummerzheim

In order to test, compare and contrast the results of the time-dependent multi-stream transport code with the results of Peticolas and Lummerzheim (2000) we calculate ionospheric electron fluxes, and 4,278 Å volume emission rates, from a source of field-aligned flux with constant intensity between 100 eV and 3 keV with 5 Hz on-off-modulation at 4,000 km. The field-aligned flux was confined to the 0° – 10° stream. For this test we used the NRLMSIS-00 neutral atmosphere (Hedin, 1991; Picone et al., 2002) for $69.58^\circ N$, $19.23^\circ E$ (location of the EISCAT Tromsø site, Tromsø, Norway, where the magnetic inclination is approximately 77°) at 22 UT 20051008, as show in Figure 1. For the collision cross-sections necessary for calculating A and B in Equations 2–7 we use the cross-sections collected by Itikawa et al. (1986), Itikawa et al. (1989) and Itikawa and Ichimura (1990), as shown in Figure 2, and to calculate the angular redistribution, modeled with p_k^x in for example, Equation 6, we use phase-functions derived from Porter et al. (1987) extended and updated with data from Linert et al. (2004) for molecular oxygen and Kanik et al. (2001) for atomic oxygen for elastic and inelastic collisions. For ionizing collisions we make the approximation that the primary high-energy electrons proceed in the forward direction and the secondary electrons produced in the ionization are isotropically distributed. Even though the neutral atmosphere and the cross-sections used here might not be exactly identical to the ones used by Peticolas and Lummerzheim (2000) the differences should be small enough to make comparisons straight-forward. The main features of electron fluxes calculated with Equation 7 agrees well with the results shown in Figures 5 and 6 of Peticolas and Lummerzheim (2000) as can be seen in Figure 3. The 4,278 Å volume-emission-rates are similar to Figure 3 of Peticolas and Lummerzheim (2000) but with a slight shift toward higher altitudes, caused by upward flux of electrons from altitudes below 150 km, as can be seen in Figures 4 and 5. This leads to a reduction of the modulation at 4,278 Å, from the 93% intensity modulation Peticolas and Lummerzheim reported, to approximately 83%. One feature that Peticolas and Lummerzheim had to simplify away which the multi-stream calculation allows us

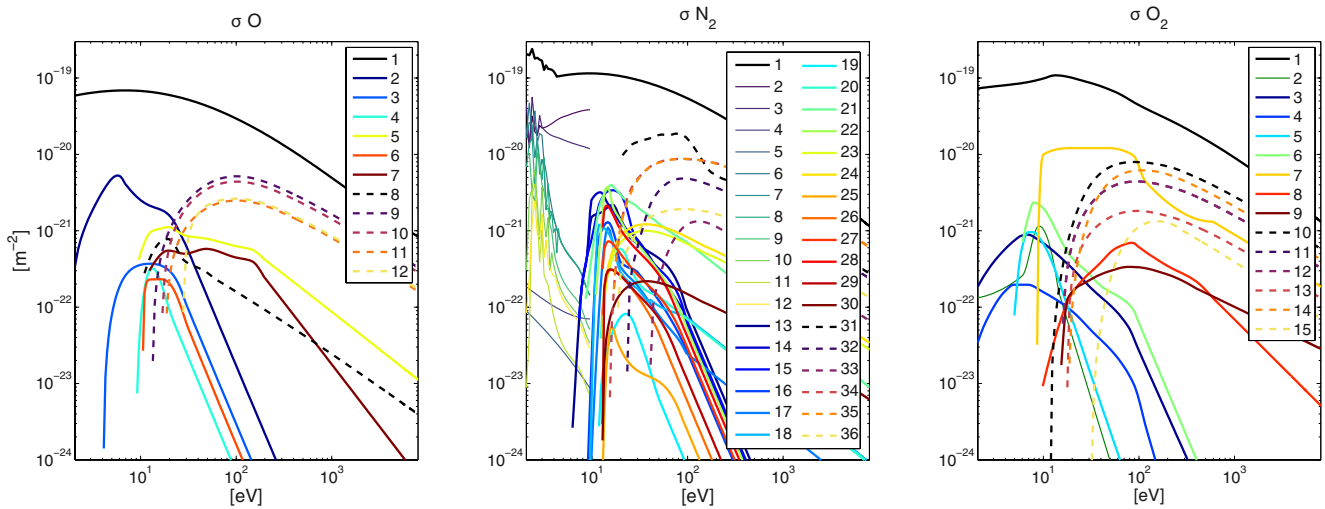


Figure 2. Electron collision cross-sections for atomic oxygen, molecular nitrogen and molecular oxygen are shown in the left, middle and right panels, respectively. The atomic oxygen cross sections are: 1 elastic, 2 $O(^1D)$, 3 $O(^1S)$, 4 $O(3s^3S_0)$, 5 $O(3s^3S_0)$, 6 $O(3p^5P)$, 7 $O(3s^3D_0)$, 8 $O(3p^3P)$, 9 $O^+(4S_0)$, 10 $O^+(2D_0)$, 11 $O^+(2P_0)$, 12 O^{++} . The molecular nitrogen cross sections are: 1 elastic, 2–5 rotational excitations 0–2, 0–4, 0–6 and 0–8, 6–12 vibrational excitations 0–1 to 0–7, 13 $N_2(A^3\Sigma_u^+)$, 14 $N_2(B^3\Pi_g)$, 15 $N_2(W^3\Delta_u)$, 16 $N_2(B'^3\Sigma_u^-)$, 17 $N_2(a'^1\Sigma_u^-)$, 18 $N_2(w^1\Delta_u)$, 19 $N_2(E^3\Sigma_g^+)$, 20 $N_2(a''^1\Sigma_g^+)$, 21 $N_2(a^1\Pi_g)$, 22 $N_2(C^3\Pi_u)$, 23 $N_2(c'^1\Sigma_u^+)$, 24 $N_2(C^3\Pi_u)$, 25 $N_2(\bar{D}^3\Sigma_u^+)$, 26 $N_2(F^3\Pi_u)$, 27 $N_2(G^3\Pi_u)$, 28 $N_2(MIM2)$, 29 $N_2(o_4^1\Pi_u)$, 30 dissociation, 31 $N + N^+$, 32 $N^+ + N^+$, 33 $N_2^+(X^2\Sigma_g^+)$, 34 $N_2^+(A^2\Pi_u)$, 35 $N_2^+(B^2\Sigma_u^+)$. The molecular oxygen cross-sections are: 1 elastic, 2 $O_2(vib)$, 3 $O_2(a^1\Delta_g)$, 4 $O_2(b^1\Sigma_g^+)$, 5 4.5 eV, 6 6 eV, 7 8.4 eV, 8 9.97 eV, 9 $O_2(3S)$, 10 $O_2(X^2\Pi_g)$, 11 $O_2^+(a^4\Pi_u)$, 12 $O_2^+(16.9eV)$, 13, $O_2^+(b^4\Sigma_g^-)$ 14, $O^+ + O$, 15, $O^+ + O^+$.

to recover is the scattering of primary electrons. This can be seen as a slow decrease of pitch-angle averaged flux after the energy-time dispersed square-wave modulated fluxes of primary field-aligned electrons above 100 eV at 490 km in Figure 3, and as angular re-distribution at 350 km, as shown in Figure 6, where primary field-aligned electrons have started scatter into all pitch-angle-streams. Further details to note in Figure 6 is that secondary

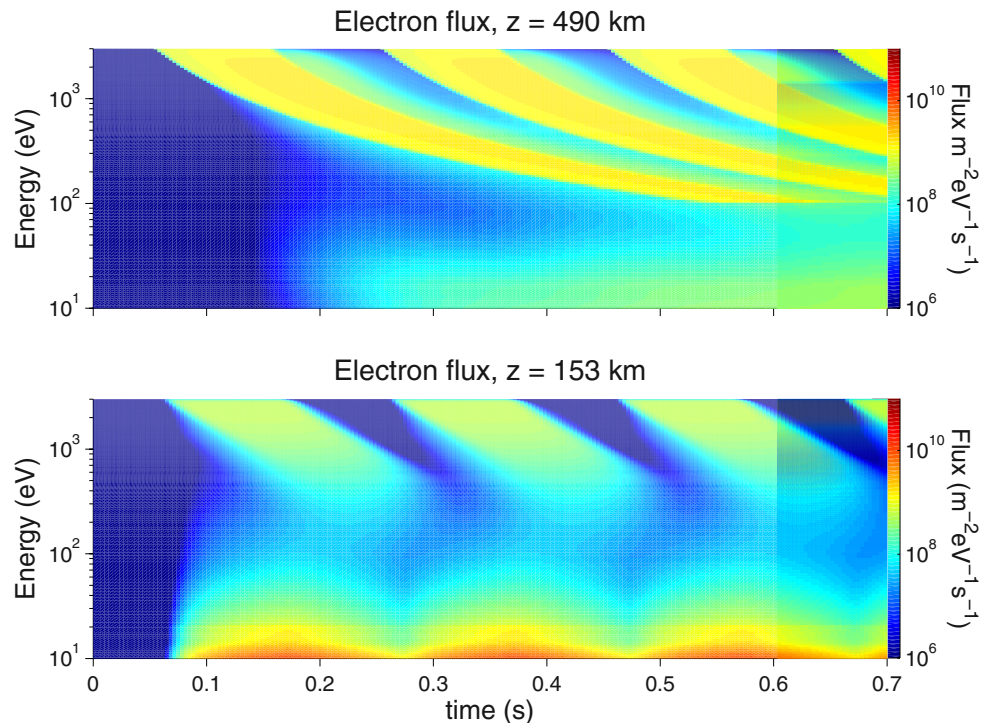


Figure 3. Time-dispersion of integral fluxes at heights of 490 and 153 km, shown in the top and bottom panel respectively, agrees well with the results in Figures 5 and 6 of Peticolas and Lummerzheim (2000).

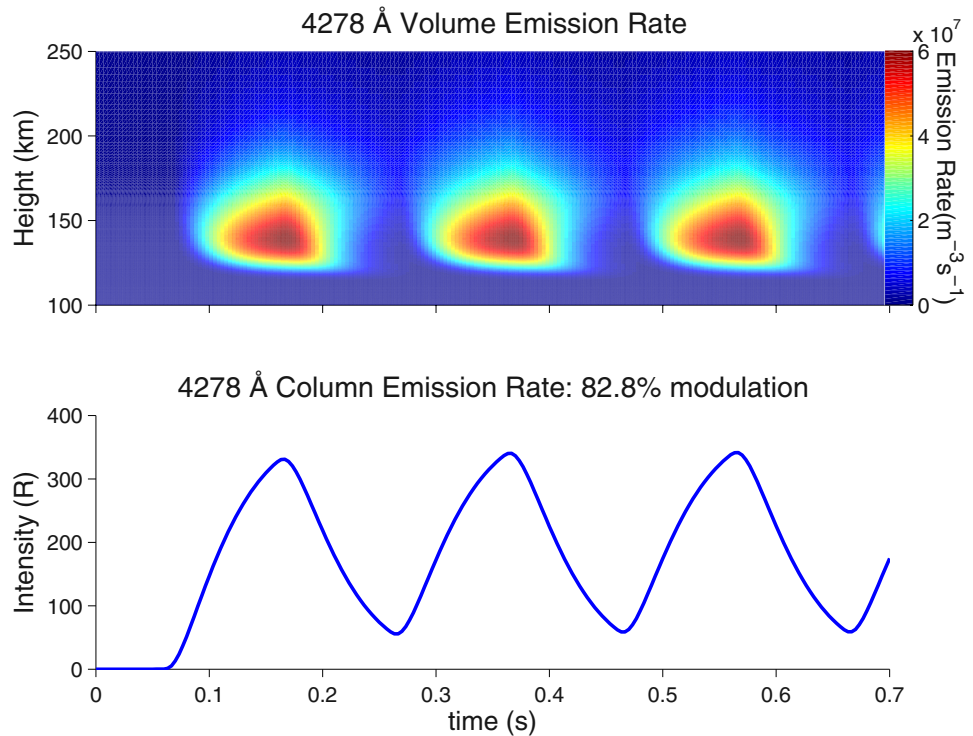


Figure 4. The volume emission at 4,278 Å from N_2^+ in the upper panel is rather similar to figure 3 of Peticolas and Lummerzheim (2000), but the modulation of the column emission-rates, shown in the bottom panel, is approximately 10 per cent smaller at 82.8%.

electrons at energies below approximately 50 eV are modulated in intensity in the 0° – 10° -beam, here the main source is time-varying production at higher altitudes; while fluxes at larger angles are slowly increasing with time, here the main source is secondary electrons from lower altitudes streaming up and scattering. The upward fluxes out of the ionosphere at energies below 100 eV, the lowest energy of the primary FAB, are a combination of secondary electrons, primarily produced at heights below 175 km and back-scattered energy-degraded primary electrons, as can be seen in Figure 5. The contribution to the albedo-flux from upward fluxes of low-energy electrons from the E-region, from below 200 km, that starts from 0.1 s is overshadowed by back-scattered primary electrons with lower energies and secondary electrons produced at higher altitudes after approximately 0.4 s. A direct consequence of the upward fluxes, is that all 10–100 eV electrons are not contained at low altitudes where the energy-degradation-time is short but some move up to altitudes above 250 km where the energy-degradation-times are significantly longer. These factors explain the reduction of the intensity modulations.

4. Flickering Flux Variations With Different Frequency and Peak Energy From Sources at Different Altitude, and the Corresponding Column Emission Rates at 4,278, 6,730, 7,774 and 8,446 Å

To further study the ionospheric response to precipitation typical for flickering aurora we have run AURORA with a range of FABs. The time and energy variation of electron fluxes in the ionosphere, and by extension the excitation and emission of auroral emissions, are controlled by the FAB peak energy, source altitude and width in energy and pitch-angle. To investigate the impact of these factors we model FAB-precipitation with constant electron-fluxes from 100 eV up to 3, 5 and 7 keV, launched from 2,000, 3,000 and 4,000 km altitude with harmonic modulation at 5, 7 and 10 Hz.

The main focus of this study is variations of column emission rates of auroral emissions, here we will present both the relative intensity modulation, IM_2 , of and the time-shift, $d\tau_{2-2}$, between emission at 4,278 Å (emitted by $N_2^+(B^2\Sigma_u^+)$), 6,730 Å ($N_2(B^3)$), 7,774 and 8,446 Å (O) as well as the O(¹D) and O(¹S) volume excitation-rates. The column emission and excitation-rates are calculated by integrating the volume emission-rates and

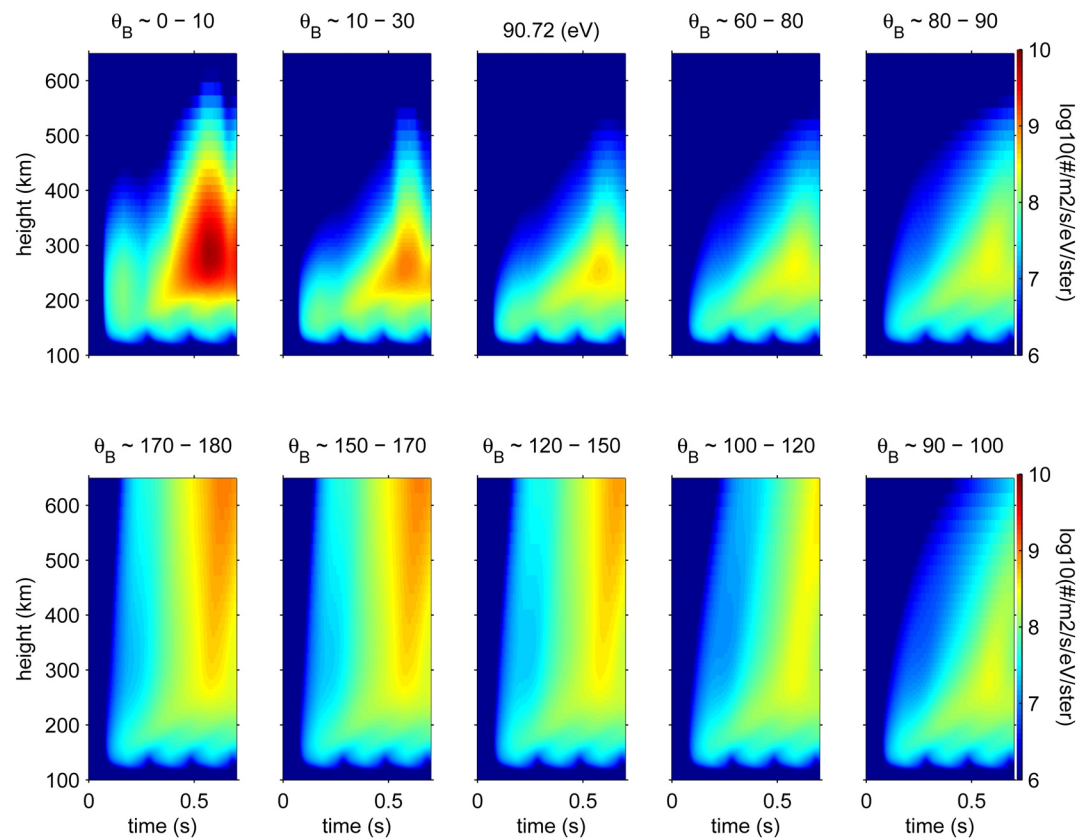


Figure 5. Time and altitude variations of 90 eV electron fluxes in the 10 streams used are shown, starting with the downward field-aligned stream in the top left panel then proceeding clockwise with increasing angle to the magnetic field to the upward field-aligned stream in the bottom left panel. In all streams the fluxes are strongly modulated only at altitudes below 150 km. Flux of energy-degraded primary electrons start to dominate the downward field-aligned flux at altitudes above 200 km from ≈ 0.4 s, while the upward fluxes start from first ionization at 120–140 km at 0.1 s; and the time-of-flight increase with the increasing angle to \mathbf{B} in the upward-going streams is due to the reduction in field-aligned velocity.

the volume emission and excitation-rates are calculated from the total differential electron fluxes. The 100 μ s photon time-of-flight across the E-region, from 140 to 110 km is only 1 order of magnitude smaller than the time-resolution extracted from AURORA, 3.33 ms, therefore the integration of the column-rates is done taking the photon-time-of-flight into account.

There are two reasons to switch from on-off to harmonic modulation of the FAB-flux at the source-altitude. The first reason is that, flickering aurora typically have intensity-variations with close to harmonic modulation (e.g., Gustavsson et al., 2008; Michell et al., 2012; Sakanoi & Fukunishi, 2004), that is, the spectral power typically decreases much faster than $1/f$ with frequency, f , above the dominant flickering frequency. Rocket and satellite observations also show precipitation with close to harmonic modulation (e.g., Arnoldy et al., 1999; McFadden et al., 1987). The second reason is that electron transport is a linear problem, that is, the differential equations describing the precipitation are all linear – therefore using harmonic modulation will give us the frequency response of the ionosphere–electron-precipitation-system, admittedly for a very limited set of the possible input parameters.

The intensity-modulation of the emissions decreases with the frequency of the electron-precipitation modulation, from 76%–64% at 5 Hz to 40%–34% at 10 Hz, as shown in Figure 7. The IM_{4278} is systematically largest, then IM_{6730} and IM_{7774} and IM_{8446} are slightly smaller. This pattern is consistent for FABs with peak energies of 3, 5 and 7 keV. For IM_{4278} there is a slight reduction with increasing peak energy, as can be seen in Figure 7. For the other emissions there are no clear IM variation with peak FAB energy.

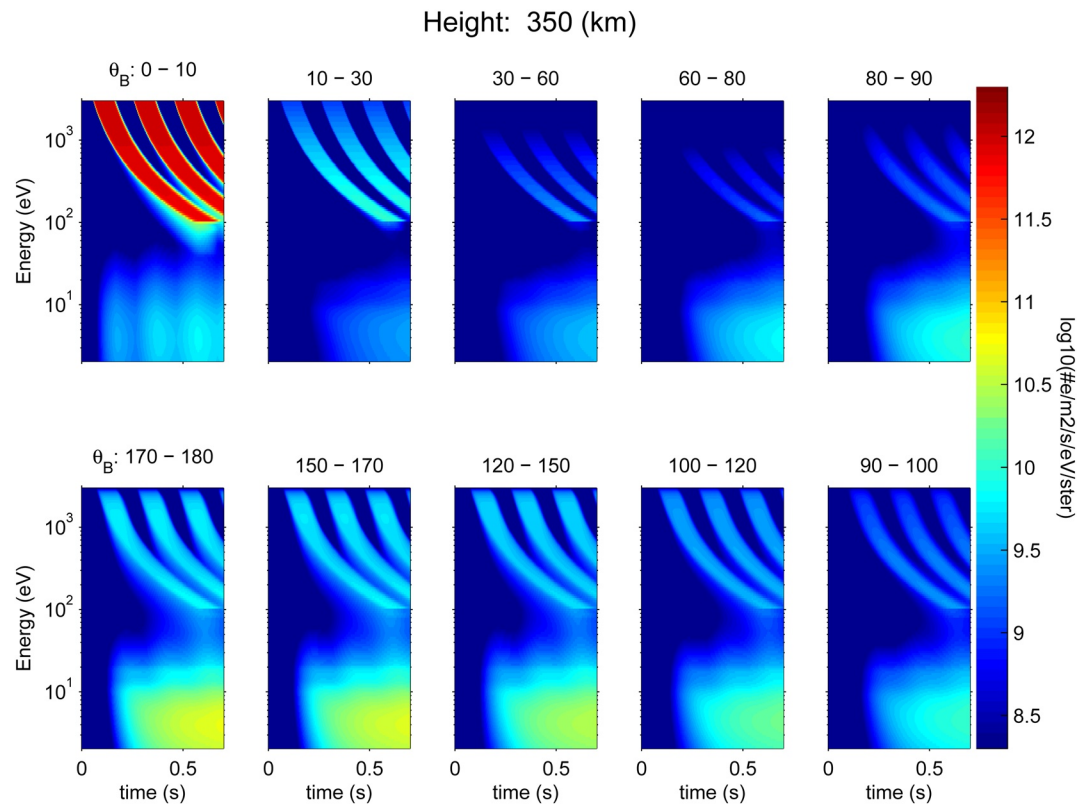


Figure 6. Time and energy-variation of electron-fluxes at 350 km altitude in the 10 streams used are shown starting with the downward field-aligned stream in the top left panel then proceeding clockwise with increasing angle to the magnetic field to the upward field-aligned stream in the bottom left panel.

When shifting the source-altitude from 2000 to 4000 km the IM_s decreases with increasing source altitude from 84%–74% to 69%–56% for 5 Hz and from 55%–44% to 36%–29% for 10 Hz, as shown in Figure 8. These reductions are entirely caused by larger velocity dispersion of the electron fluxes due to the increased time-of-flight differences.

There are time-shifts between intensity-maxima of the different emissions, τ_λ^M , and the intensity minima, τ_λ^m . For FABs starting from 3,000 km with peak energy of 5 and 7 keV the time-shifts are reasonably constant, $d\tau_{6730-4278}$ varies between 10 and 13.3 ms, $d\tau_{7774-4278}$ varies between 3.3 and 6.7 ms, and $d\tau_{8446-4278}$ varies between 0 and 3.3 ms. For FABs with 3 keV peak energy there seems to be a slight decrease with increasing frequency for all three time-shifts with $d\tau_{6730-4278}$ decreasing from 13.3 ms at 5 Hz to 10 ms at 10 Hz, $d\tau_{7774-4278}$ decreases from 6.7 to 3.3 ms, and $d\tau_{8446-4278}$ decreases from 3.3 to 0 ms.

5. Discussion

The variations of intensity modulations of and time-shifts between the different emissions can be understood, with varying levels of effort. That the intensity modulations decrease with increasing source-altitude can be easily understood since there will be an increased velocity dispersion. Likewise the reduction in intensity modulation with increased frequency can be easily explained with the shortened time between peaks in the precipitation and an increasing overlap between the low and high-energy tails of consecutive FABs leading to reduced variation of the ionospheric electron-fluxes. The impact of pitch-angle distribution cannot be well resolved, due to the coarse pitch-angle resolution; here we calculate IM for a pitch-angle distribution with equal number of electrons in the 0°–10°, 10°–30° and 30°–60° beams. This gives IM that decreases with wider pitch-angle spread, as can be seen in Figure 8. Here it should be noted that the current version of AURORA ignores the magnetic mirror-force in the ionosphere and other forces between the source-region and the top of the ionosphere. This simplification has a negligibly small effect for close to field-aligned precipitation, but for wider pitch-angle distributions

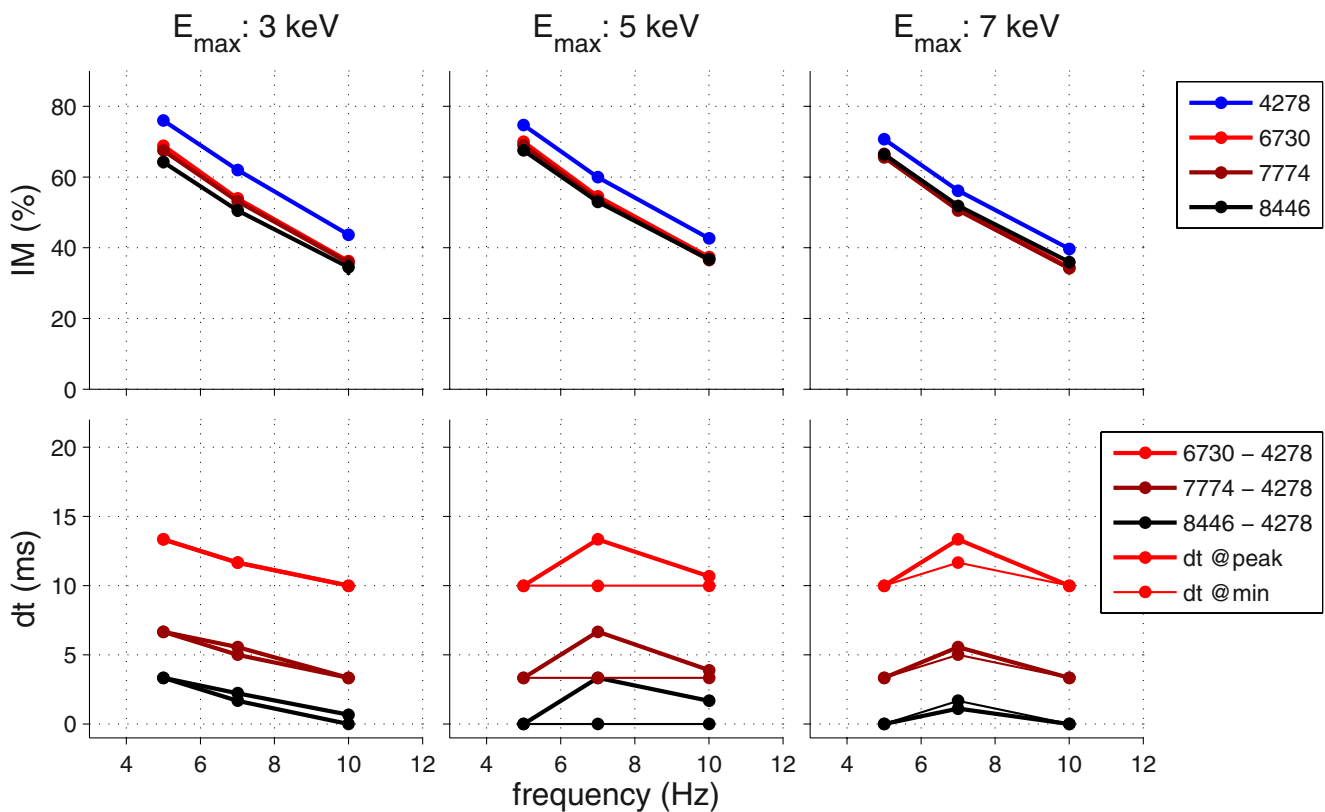


Figure 7. Frequency variation of intensity modulation for emissions at 4,278, 6,730, 7,774 and 8,446 Å produced by field-aligned bursts (FAB) with peak-energy at 3, 5 and 7 keV are displayed in the top left, top middle and top right panels respectively. In the bottom panels the lag-time from the maxima (thick lines) and minima (thin lines) of the emission in 4,278 Å to the maxima (minima) in the 6,730, 7,774, and 8,446 Å emissions are plotted.

the effect will become significant. Electrons with 30° pitch-angle at 600 km altitude will, have pitch-angles of approximately 23°, 19° and 16° at 2,000, 3,000 and 4,000 km, just due to the magnetic mirror-force. Ignoring the pitch-angle-variation with altitude leads to an increase in time-of-arrival with 3%–7%. For electrons with 60° pitch-angle at 600 km, the time-of-arrival error increases to between 27% and 46%.

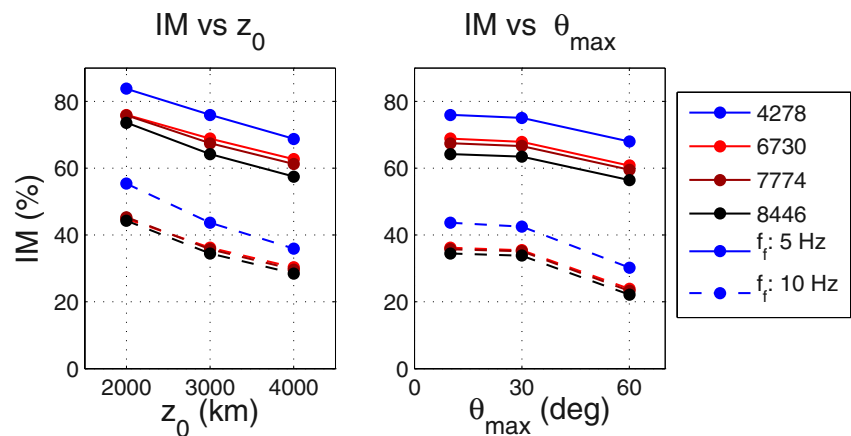


Figure 8. The intensity modulation variations with source altitude is plotted in the left panel for FABs with 3 keV peak energy modulated at 5 and 10 Hz, where systematic intensity modulation reductions can be seen. In the right panel the intensity modulation amplitude variation with pitch-angle width is plotted for FABs with 3 keV peak energy launched from a source altitude of 3,000 km.

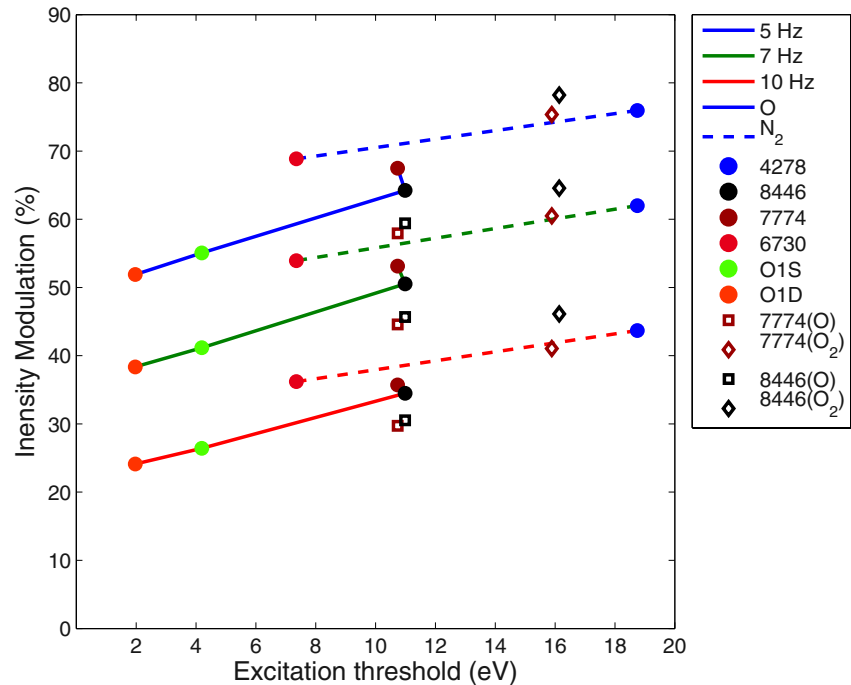


Figure 9. Modulation amplitudes of emissions (and excitation for O(¹S) and O(¹D)) produced by harmonically modulated FABs with 3 keV maximum energy from 3,000 km altitude as a function of excitation threshold are plotted for modulation frequencies of 5, 7 and 10 Hz. Here it is worth noting that the modulation of the 7,774 and 8,446 Å source from dissociative excitation of molecular oxygen falls in line with the molecular nitrogen-(ion) emissions and are larger than the direct electron impact excitation of atomic oxygen.

The two main factors affecting the differences between IM of different emissions, as shown in Figure 9, are the excitation threshold and the altitude profile of the excited species. Excited states with lower excitation threshold should have a relatively larger contribution from low-energy electrons, which are weakly modulated at altitudes above 175 km, as can be seen in Figure 5 and in the supplementary animation that shows how the electron-fluxes as a function of energy and altitude varies with time. Since atomic oxygen has a larger scale-height than molecular nitrogen, that in turn has a larger scale-height than molecular oxygen, direct electron impact excitation of atomic oxygen should have a smaller modulation since it will have a relatively larger contribution from higher altitudes where the electron-flux modulation is lower. Since both states that emits at 7,774 and 8,446 Å are produced by direct electron impact excitation of O and of dissociative excitation of molecular oxygen the emissions should have one source with large and one source with small IM. This can be seen in the time-variations of the relative intensities presented in Figure 10, where the IM at 6,730 Å is smaller than at 4,278 Å, and both the trend of decreasing IM with decreasing excitation threshold and the larger IM for the dissociative excitation of O₂ than the direct excitation of O are clearly visible. Typically the observed flickering amplitude is on the order of 10% of the total brightness (e.g., Whiter et al., 2008, 2010). With the 40%–75% IM obtained from FABs here this implies that the total energy-flux in the FABs has to be on the order of 15%–25% of the total energy-flux, this is a large fraction considering the narrow pitch-angle width of FABs.

There will be a time-lag of the low-energy-flux variation at higher altitudes relative to the electron-fluxes at lower altitudes, due to the longer energy-degradation-time and the delayed time-of-arrival of the low-energy tail of the FABs; the time-shifts between the different emissions can be explained in a similar way. Excitation of states with low excitation threshold, with a relatively larger contribution from excitation by low-energy electrons with the time-shifted modulation, should have a larger time-shift than states with higher excitation threshold; and that emissions (excitation in the case of O(¹D) and O(¹D)) from atomic oxygen should have larger time-shifts relative to emissions from molecular nitrogen, since the production of excited oxygen states have a relatively larger contribution from higher altitudes where the excitation have a larger time-shift than at lower altitudes. The 7,774 and 8,446 Å emissions have sources from electron collisions with O and O₂, the intensity variations should have one component with larger IM and smaller time-shift and one component with smaller IM and larger time-shift.

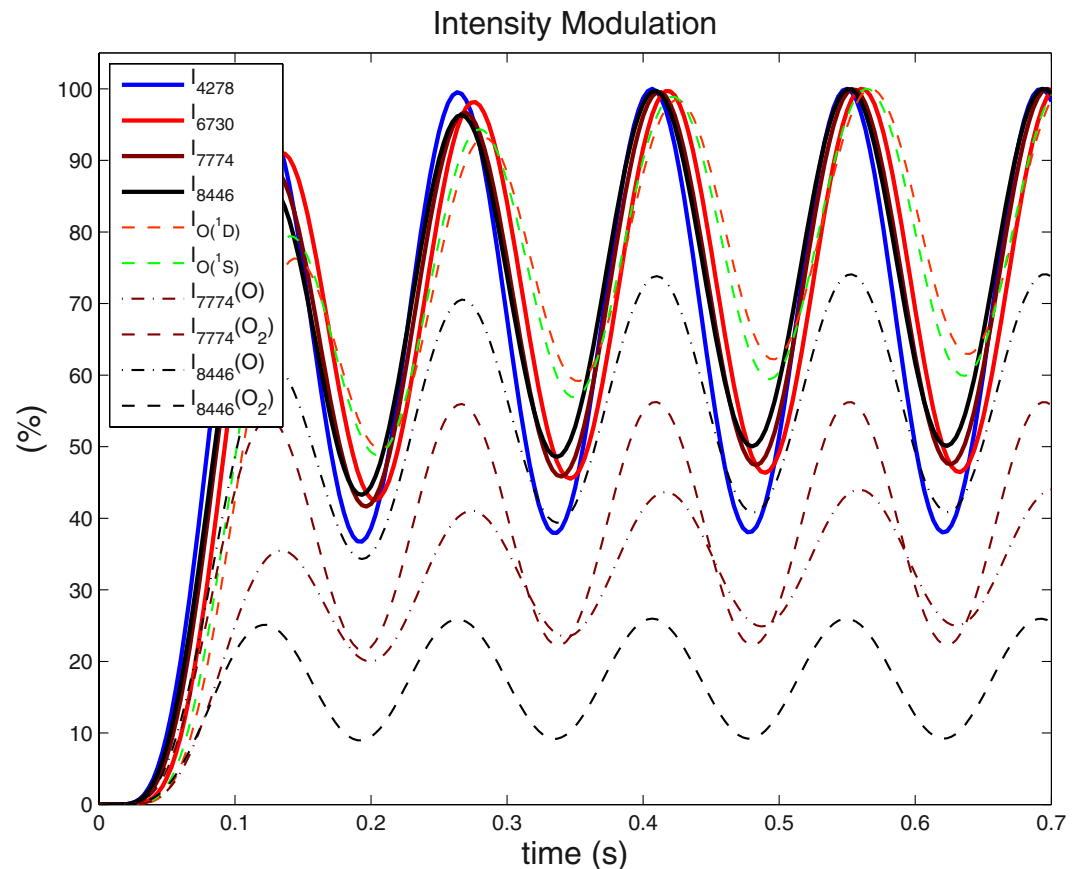


Figure 10. Time evolution of the relative intensity variations for the four column-emission rates and the column excitation rates for $O(^1D)$ and $O(^1S)$ produced by Field-aligned bursts with 3 keV peak energy modulated at 7 Hz at 3,000 km show variation in both IM and time-shifts. For clarity the contribution from the two sources to I_{7774} and I_{8446} are plotted normalized to the peak intensity in respective emission.

This can be clearly seen in Figure 10 where the intensity variation of the 7,774 source from dissociative excitation of O_2 is clearly larger and with a smaller time-shift, than the direct electron impact excitation of O that has the larger time-shift.

Comparisons between the results of AURORA and a time-dependent Monte-Carlo-based electron transport code would be of great interest. The two methods have complementary strengths, AURORA is free from stochastic counting-noise, and Monte-Carlo methods does not have a finite pitch-angle-stream approximation.

6. Summary and Predictions

We have developed a time-dependent multi-stream electron transport code, AURORA, suitable for studies of aurora with sub-second dynamics. This transport code accurately takes into account the discrete energy-losses in inelastic collisions and pitch-angle scattering in elastic and inelastic collisions. As currently used there are two simplifications: that the production of secondary electrons is isotropic, and that the high-energy primary electrons are scattered in the forward direction in ionizing collisions. This is done for computational speed and is a reasonable approximation since only a small fraction of secondary electrons are produced at energies close to half the energy of the primary electrons where the production of secondary electrons is not close to isotropic. Further, the 10 pitch-angle streams that currently are feasible to use makes it difficult to accurately model smooth medium-wide pitch-angle distributions. These simplifications can be adjusted as computational resources improve.

We used AURORA to study FABs in flickering aurora. The 4,278 Å emission modulation produced by a 5 Hz on-off modulated FAB launched from 4,000 km with 3 keV peak energy is 83%, which is 10% less than what the

Peticolas and Lummerzheim (2000)-model produced. This is primarily explained by the upward transport of secondary electrons to altitudes above 175 km where their energy-degradation-time is significantly longer than 0.1 s, which leads to a background source of excitation with smaller modulation. A thorough investigation of the ionospheric response to harmonically modulated FABs at 5, 7 and 10 Hz with peak energies of 3, 5 and 7 keV, launched from 2,000, 3,000 and 4,000 km show that the intensity modulation is reduced with increasing source altitude and modulation frequency. The variation with source-altitude is due to the increased velocity dispersion, and the variation with frequency is due to increasing overlap between consecutive bursts. The intensity modulation varies only weakly with the peak-energy of the FABs. Further, the calculations show that the intensity modulation at 6,730, 7,774 and 8,446 Å are rather similar, and slightly lower than at 4,278 Å. The primary reason for this variation is that the emissions with lower excitation threshold have a relatively larger contribution from un-modulated low-energy electron flux above 175 km, this effect is larger for emissions from atomic oxygen due to its larger thermospheric scale-height. The model calculations also predicts that there should be a time-shift between different emissions, with the 6,730, 7,774 and 8,446 Å emissions being approximately 10, 5 and 3 ms delayed relative to the 4,278 Å emission, respectively. The time-shifts between the different emissions should be detectable with multi-monochromatic high-speed imaging – provided that the camera synchronization have better accuracy than ≈ 100 μ s.

Data Availability Statement

This manuscript contains no primary data. The time-dependent multi-stream electron transport code AURORA is available under the GNU copyleft licence from the author.

Acknowledgments

We would like to thank Laura Peticolas and Dirk Lummerzheim for their work that inspired this effort, and Tima Sergienko for contributing with phase-functions and cross-sections.

References

- Arnoldy, R. L., Lynch, K. A., Austin, J. B., & Kintner, P. M. (1999). Energy and pitch angle-dispersed auroral electrons suggesting a time-variable, inverted-V potential structure. *Journal of Geophysical Research*, *104*(A10), 22613–22622. <https://doi.org/10.1029/1999JA900219>
- Blixt, E. M., Grydeland, T., Ivchenko, N., Hagfors, T., La Hoz, C., Lanchester, B. S., et al. (2005). Dynamic rayed aurora and enhanced ion-acoustic radar echoes. *Annales Geophysicae*, *23*(1), 3–11. <https://doi.org/10.5194/angeo-23-3-2005>
- Dahlgren, H., Aikio, A., Kaila, K., Ivchenko, N., Lanchester, B., Whiter, D., & Marklund, G. (2010). Simultaneous observations of small multi-scale structures in an auroral arc. *Journal of Atmospheric and Solar-Terrestrial Physics*, *72*(7–8), 633–637. <https://doi.org/10.1016/j.jastp.2010.01.014>
- Dahlgren, H., Semeter, J., Marshall, R., & Zettergren, M. (2013). The optical manifestation of dispersive field-aligned bursts in auroral breakup arcs. *Journal of Geophysical Research: Space Physics*, *118*(7), 4572–4582. <https://doi.org/10.1002/jgra.50415>
- Fang, X., Randall, C. E., Lummerzheim, D., Wang, W., Lu, G., Solomon, S. C., & Frahm, R. A. (2010). Parameterization of monoenergetic electron impact ionization. *Geophysical Research Letters*, *37*(22), L22106. <https://doi.org/10.1029/2010GL045406>
- Gattinger, R. L., Llewellyn, E. J., & Vallance Jones, A. (1996). On I(5577 Å) and I(7620 Å) auroral emissions and atomic oxygen densities. *Annales Geophysicae*, *14*(7), 687–698. <https://doi.org/10.1007/s00585-996-0687-1>
- Gronoff, G., Simon Wedlund, C., Mertens, C. J., & Lillis, R. J. (2012). Computing uncertainties in ionosphere-airglow models: I. Electron flux and species production uncertainties for Mars. *Journal of Geophysical Research*, *117*(A4), A04306. <https://doi.org/10.1029/2011JA016930>
- Grydeland, T., Blixt, E. M., Løvhaug, U. P., Hagfors, T., La Hoz, C., & Trondsen, T. S. (2004). Interferometric radar observations of filamented structures due to plasma instabilities and their relation to auroral rays. *Annales Geophysicae*, *22*(4), 1115–1132. <https://doi.org/10.5194/angeo-22-1115-2004>
- Guio, P. (1998). *Studies of ionospheric parameters by means of electron plasma lines observed by EISCAT*. (Unpublished doctoral dissertation). University of Tromsø. Retrieved from <https://hdl.handle.net/10037/2976>
- Gustavsson, B., Lunde, J., & Blixt, E. M. (2008). Optical observations of flickering aurora and its spatio-temporal characteristics. *Journal of Geophysical Research*, *113*(A12), A12317. <https://doi.org/10.1029/2008ja013515>
- Hedin, A. (1991). Extension of the MSIS thermospheric model into the middle and lower atmosphere. *Journal of Geophysical Research*, *96*(A2), 1159–1172. <https://doi.org/10.1029/90ja02125>
- Itikawa, Y., Hayashi, M., Ichimura, A., Onda, K., Sakimoto, K., Takayanagi, K., et al. (1986). Cross sections for collisions of electrons and photons with nitrogen molecules. *Journal of Physical and Chemical Reference Data*, *15*(3), 985–1010. <https://doi.org/10.1063/1.555762>
- Itikawa, Y., & Ichimura, A. (1990). Cross sections for collisions of electrons and photons with atomic oxygen. *Journal of Physical and Chemical Reference Data*, *19*(3), 637–651. <https://doi.org/10.1063/1.555857>
- Itikawa, Y., Ichimura, A., Onda, K., Sakimoto, K., Takayanagi, K., Hatano, Y., et al. (1989). Cross sections for collisions of electrons and photons with oxygen molecules. *Journal of Physical and Chemical Reference Data*, *18*(1), 23–42. <https://doi.org/10.1063/1.555841>
- Kanik, I., Johnson, P. V., Das, M. B., Khakoo, M. A., & Tayal, S. S. (2001). Electron-impact studies of atomic oxygen: I. Differential and integral cross sections; experiment and theory. *Journal of Physics B: Atomic and Molecular Physics*, *34*(13), 2647–2665. <https://doi.org/10.1088/0953-4075/34/13/308>
- Kataoka, R., Miyoshi, Y., Sakanoi, T., Yaegashi, A., Ebihara, Y., & Shiohara, K. (2011). Ground-based multispectral high-speed imaging of flickering aurora. *Geophysical Research Letters*, *38*(14), L14106. <https://doi.org/10.1029/2011GL048317>
- Linert, I., King, G. C., & Zubek, M. (2004). Measurements of differential cross sections for elastic electron scattering in the backward direction by molecular oxygen. *Journal of Physics B: Atomic and Molecular Physics*, *37*(23), 4681–4691. <https://doi.org/10.1088/0953-4075/37/23/009>
- Lummerzheim, D., & Liliensten, J. (1994). Electron transport and energy degradation in the ionosphere: Evaluation of the numerical solution, comparison with laboratory experiments and auroral observations. *Annales Geophysicae*, *12*(10), 1039–1051. <https://doi.org/10.1007/s00585-994-1039-7>

- McFadden, J. P., Carlson, C. W., Boehm, M. H., & Hallinan, T. J. (1987). Field-aligned electron flux oscillations that produce flickering aurora. *Journal of Geophysical Research*, *92*(A10), 11133–11148. <https://doi.org/10.1029/ja092ia10p11133>
- Michell, R., McHarg, M., Samara, M., & Hampton, D. (2012). Spectral analysis of flickering aurora. *Journal of Geophysical Research*, *117*(A3), A03321. <https://doi.org/10.1029/2011ja016703>
- Peticolas, L., & Lummerzheim, D. (2000). Time-dependent transport of field-aligned bursts of electrons in flickering aurora. *Journal of Geophysical Research*, *105*(A6), 12895–12906. <https://doi.org/10.1029/1999ja000398>
- Picone, J. M., Hedin, A. E., Drob, D. P., & Aikin, A. C. (2002). NRLMSISE-00 empirical model of the atmosphere: Statistical comparisons and scientific issues. *Journal of Geophysical Research*, *107*(A12), 1468. <https://doi.org/10.1029/2002JA009430>
- Porter, H. S., Varosi, F., & Mayr, H. G. (1987). Iterative solution of the multistream electron transport equation: 1. Comparison with laboratory beam injection experiments. *Journal of Geophysical Research*, *92*(A6), 5933–5959. <https://doi.org/10.1029/ja092ia06p05933>
- Rees, M. H. (1989). *Physics and chemistry of the upper atmosphere* (In J. T. Houghton, M. J. Rycroft, & A. J. Dessler (Eds.)), Cambridge University Press.
- Sakanoi, K., & Fukunishi, K. (2004). Temporal and spatial structures of flickering aurora derived from high-speed imaging photometer observations at Syowa Station in the Antarctic. *Journal of Geophysical Research*, *109*(A1), A01221. <https://doi.org/10.1029/2003JA010081>
- Schunk, R., & Nagy, A. (2009). *Ionospheres: Physics, plasma physics, and chemistry*. Cambridge university press.
- Semeter, J., & Blixt, E. M. (2006). Evidence for Alfvén wave dispersion identified in high-resolution auroral imagery. *Geophysical Research Letters*, *33*(13), 13106. <https://doi.org/10.1029/2006GL026274>
- Sergienko, T. I., & Ivanov, V. E. (1993). A new approach to calculate the excitation of atmospheric gases by auroral electron impact. *Annales Geophysicae*, *11*, 717–727.
- Solomon, S. (1993). Auroral electron transport using the Monte Carlo method. *Geophysical Research Letters*, *20*(3), 185–188. <https://doi.org/10.1029/93gl00081>
- Stamnes, K. (1981). On the two-stream approach to electron transport and thermalization. *Journal of Geophysical Research*, *86*(A4), 2405–2410. <https://doi.org/10.1029/ja086ia04p02405>
- Strickland, D. J., Meier, R. R., Hecht, J. H., & Christensen, A. B. (1989). Deducing composition and incident electron spectra from ground-based auroral optical measurements: Theory and model results. *Journal of Geophysical Research*, *94*(A10), 13527–13539. <https://doi.org/10.1029/ja094ia10p13527>
- Swartz, W. E., Nisbet, J. S., & Green, A. E. S. (1971). Analytic expression for the energy-transfer rate from photoelectrons to thermal electrons. *Journal of Geophysical Research*, *76*(34), 8475–8480. <https://doi.org/10.1029/ja076i034p08425>
- Vogt, J., Frey, H. U., Haerendel, G., Höfner, H., & Semeter, J. L. (1999). Shear velocity profiles associated with auroral curls. *Journal of Geophysical Research*, *104*(A8), 17277–17288. <https://doi.org/10.1029/1999ja900148>
- Whiter, D. K., Lanchester, B. S., Gustavsson, B., Ivchenko, N., & Dahlgren, H. (2010). Using multispectral optical observations to identify the acceleration mechanism responsible for flickering aurora [Article]. *Journal of Geophysical Research*, *115*(A12), A12315. <https://doi.org/10.1029/2010JA015805>
- Whiter, D. K., Lanchester, B. S., Gustavsson, B., Ivchenko, N., Sullivan, J. M., & Dahlgren, H. (2008). Small-scale structures in flickering aurora. *Geophysical Research Letters*, *35*(23), L23103. <https://doi.org/10.1029/2008GL036134>